Applied Surface Science 737 (2026) 166846

Contents lists available at ScienceDirect

Applied Surface Science

journal homepage: www.elsevier.com/locate/apsusc

Full Length Article

# Atomic-scale evidence of Sb interdiffusion driving irreversible surface phase transition in $MA_3Sb_2I_9$ lead-free perovskites

Seungwoo Yoo [a,1], Young Mi Lee [b,1], Seungjun Lee [a,2], Inhee Maeng [c], Jae Ho Kim [d], Yuya Yoshie [e], Sakura Nishino Takeda [e], Masakazu Nakamura [e], Zhe Sun [f], Seung Jae Oh [c], Myungkwan Song [d], Shenghao Wang [g,h,*], Min-Cherl Jung [i,**], Young-Kyun Kwon [a,j,***]

[a] Department of Physics and Research Institute for Basic Sciences, Kyung Hee University, Seoul 02447, the Republic of Korea
[b] Beamline Department, Pohang Accelerator Laboratory, POSTECH, Pohang 37673, the Republic of Korea
[c] YUHS-KRIBB, Medical Convergence Research Institute, College of Medicine, Yonsei University, Seoul 03722, the Republic of Korea
[d] Department of Energy & Electronic Materials, Korea Institute of Materials Science (KIMS), Changwon 51508, the Republic of Korea
[e] Division of Materials Science, Nara Institute of Science and Technology, Nara 630-0192, Japan
[f] National Synchrotron Radiation Laboratory, University of Science and Technology of China, Hefei 230029, China
[g] School of Materials Science and Engineering, Hainan University, Haikou 570228, China
[h] Materials Genome Institute (MGI), Shanghai University, Shanghai 200444, China
[i] Global Institute of Future Technology, Shanghai Jiao Tong University, Shanghai 200240, China
[j] Department of Information Display, Kyung Hee University, Seoul 02447, the Republic of Korea

ARTICLE INFO

*Keywords:*
Lead-free perovskites
Sb interdiffusion
Irreversible surface degradation
Photoemission spectroscopy (PES)
Density functional theory (DFT)

ABSTRACT

Cooling, rather than annealing, drives surface-to-bulk Sb interdiffusion that irreversibly reconstructs $MA_3Sb_2I_9$ surfaces. In situ photoemission spectroscopy (PES) and reflection high-energy electron diffraction across the full thermal cycle show that annealing sharpens diffraction streaks and partially depletes surface methylammonium (MA), whereas cooling removes Sb-related spectral features and collapses the streaks. Density-of-states calculations including spin–orbit coupling reproduce the PES evolution, and *ab initio* molecular dynamics reveal the atomistic mechanism associated with Sb-deficient configurations: local Sb-I coordination collapses and covalent I-I bonds form upon Sb depletion. Treating MA depletion during annealing and Sb interdiffusion during cooling as separate steps explains the observed irreversibility and reconciles mixed reports on $A_3B_2X_9$ processing. The mechanism provides practical guidance for stabilizing lead-free perovskite surfaces, including passivation before cool-down, halide-rich surface chemistries, and reduced thermal gradients. Beyond $MA_3Sb_2I_9$, this cooling-aware approach offers transferable rules for processing and reliability in antimony-based, lead-free perovskites.

## 1. Introduction

Lead-free halide perovskite-related materials have attracted considerable attention for next-generation optoelectronics, combining strong light–matter interactions with scalable processing across photovoltaics [1], light-emitting devices [2], and THz detection [3]. At the same time, the toxicity of lead in conventional perovskites has driven sustained efforts toward environmentally benign alternatives [4–6]. Within this broader context, $MA_3Sb_2I_9$ is an appealing antimony-based vacancy-ordered perovskite derivative belonging to the $A_3B_2X_9$ family, in which Sb adopts the + 3 oxidation state [7–9]. Unlike conventional $ABX_3$ perovskites, $MA_3Sb_2I_9$ exhibits rich structural polymorphism with both 0D dimeric [7] and 2D layered [8] motifs (see Fig. S1a for detailed atomic structures). These distinct structural characteristics make $MA_3Sb_2I_9$ a useful platform for investigating how structural dimensionality influences electronic properties and surface stability under thermal processing. At the same time, its surface chemistry remains far less understood than its bulk structural and optoelectronic properties,

* Corresponding author at: School of Materials Science and Engineering, Hainan University, Haikou 570228, China.
** Corresponding author.
*** Corresponding author at: Department of Physics and Research Institute for Basic Sciences, Kyung Hee University, Seoul 02447, the Republic of Korea.
*E-mail addresses:* shenghao.wang@hainanu.edu.cn (S. Wang), mincherl.jung@sjtu.edu.cn (M.-C. Jung), ykkwon@khu.ac.kr (Y.-K. Kwon).
[1] These authors contributed equally: Seungwoo Yoo and Young Mi Lee.
[2] Current address: Department of Applied Physics, Kyung Hee University, Yongin 17104, Republic of Korea.

https://doi.org/10.1016/j.apsusc.2026.166846
Received 26 December 2025; Received in revised form 1 April 2026; Accepted 7 April 2026
Available online 13 April 2026

despite the central role of surfaces in determining the performance and long-term stability of perovskite-based materials.

Because device performance is governed by surface chemistry, reconstruction, and defect formation, a surface-focused understanding of $MA_3Sb_2I_9$ is essential. This issue is particularly important under realistic thermal protocols, since annealing and subsequent cooling can induce structural and electronic changes in related halide systems [10–16]. Despite significant progress in $A_3B_2X_9$ chemistry, including phase control, thin-film preparation, and stability mapping, the surface-specific evolution of $MA_3Sb_2I_9$ during annealing and subsequent cooling remains comparatively underexplored, partly because the orientational dynamics of the methylammonium (MA) cation complicate theory and experiment [17–22]. Addressing this problem also demands high-quality samples that present atomically ordered surfaces with low defect densities suitable for surface-sensitive probes. Here we adopt growth and handling routes that yield such high-quality $MA_3Sb_2I_9$ surfaces, as indicated by streak-like reflection high-energy electron diffraction (RHEED) and narrow core-level features, and we build on our prior experience with high-quality crystals and films in related perovskite systems [22–24].

This work delivers a balanced experiment–theory analysis. From the experimental side, we track the full thermal cycle in situ using high-resolution photoemission spectroscopy (PES) and RHEED. Annealing sharpens diffraction streaks and partially depletes surface MA; cooling removes Sb-related spectral signatures and collapses the sharpened streaks. From the theoretical side, we employ electronic-structure calculations that include spin–orbit coupling (SOC) effects to reproduce the PES evolution and finite-temperature molecular dynamics to reveal short-range coordination changes. Full computational details are provided in Experiments and Computations and the ESI.

Crucially, the combined analysis is required for a new interpretation: cooling, rather than annealing, is the decisive step that drives surface-to-bulk Sb interdiffusion, collapses local Sb-I coordination, and promotes I-I bond formation. Separating the two temperature windows clarifies the sequence: annealing produces near-surface MA depletion coincident with improved surface order; subsequent cooling drives Sb interdiffusion into the bulk, which explains the observed irreversibility and reconciles mixed reports on thermal processing in $A_3B_2X_9$ systems. By resolving the temperature-dependent atomistic mechanism associated with Sb-deficient surface evolution, this joint experimental-computational framework also suggests actionable guidelines—passivation before cool-down, halide-rich surface chemistries, and reduced thermal gradients—to stabilize lead-free antimony perovskite surfaces. Together, our results establish a cooling-aware view of surface control in $MA_3Sb_2I_9$: the dominant degradation pathway is activated during cool-down rather than during annealing, and the principle is likely general across $A_3B_2X_9$ perovskites.

## 2. Experiments and computations

### 2.1. Single-crystal preparation

$CH_3NH_3I$ (MAI) was synthesized by dissolving methylamine (27.8 mL) in anhydrous methanol (30 mL, Sigma-Aldrich, 99.8%), cooling the solution below 275 K in an ice bath, and slowly adding hydroiodic acid (12.7 mL, Sigma Aldrich, 57 wt% in $H_2O$). After 2 h stirring the product was concentrated by rotary evaporation, recrystallized from diethyl ether (Fisher Scientific, 99.99%), and dried overnight in a vacuum oven. $MA_3Sb_2I_9$ precursor solutions were then prepared by dissolving MAI (handmade) and $SbI_3$ (Sigma-Aldrich, 98%) in anhydrous methanol (Sigma-Aldrich, 99.8%) at 3:2 M ratio stirred for 8 h, filtered through a 0.45 μm polytetrafluoro-ethylene (PTFE) filter, and adjusted to 0.01 M. Numerous small seeds (≈1–2 mm) formed after 24 h at room temperature (RT). For large single crystals, a single seed was transferred to fresh solution and grown at 60 °C for 2 days; this step was repeated until the target size was reached. (See the inset of Fig. 1)

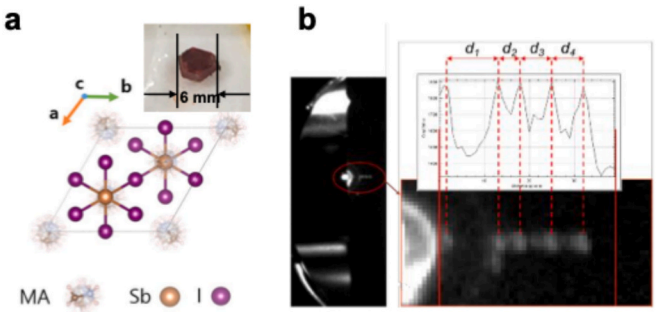


**Fig. 1.** (a) Atomic structure of 0D $MA_3Sb_2I_9$, highlighting the rotational freedom of MA cations, which influences the material's dynamic properties. The inset image is the single crystal sample synthesized. (b) RHEED pattern of $MA_3Sb_2I_9$ after annealing, demonstrating improved surface crystallinity. The diffraction pattern exhibits surface-projected periodicities compatible with hexagonal symmetry.

### 2.2. RHEED

To assess surface crystallinity, reflection high-energy electron diffraction was performed at RT. Surfaces were freshly cleaved with a clean blade before loading and then mounted on a Si(111) stage. Post-annealing was applied in vacuo at 373 K for 10 min by passing 97 mA through the Si(111) stage; the surface temperature was verified by a UV spectrometer. The base pressure was $1.1 \times 10^{-7}$ Torr. Typical RHEED conditions were 15 kV beam energy, 20 μA current, and 0.5° incidence. RHEED was used qualitatively to indicate improved surface crystallinity; no bulk lattice constants were extracted

### 2.3. High-resolution PES

Photoemission measurements were carried out at BL-13U (NSRL) using a Scienta Omicron DA30L analyzer. The total energy resolution was better than 15 meV and the angular resolution was 0.3°. Flat, mirror-like surfaces were obtained by in situ cleavage, followed by a mild post-anneal at 360 K under a base pressure better than $2.9 \times 10^{-10}$ Torr. Spectra were referenced to the Fermi level ($E_F$) of a metallic standard measured in identical geometry and processed with standard background and doublet fitting procedures [25]. Additional instrumental settings (photon energies, incidence angles, scan ranges) and the anneal/cool protocol are summarized in the ESI

### 2.4. Electronic-structure calculations

Density-functional theory (DFT) was used to interpret the PES evolution and isolate bonding changes [26–28]. Calculations were performed using Vienna *ab initio* simulation package (VASP) [29,30] with projector-augmented-wave pseudopotentials [31,32], using the following valence electron configurations: $4d^{10}5s^25p^3$ for Sb, $5s^25p^5$ for I, $2s^22p^3$ for N, $2s^22p^2$ for C, and $1\ s^1$ for H. A plane-wave cutoff of 400 eV was employed together with the Perdew, Burke, and Ernzerhof exchange–correlation functional [33] and Grimme's DFT-D3 dispersion correction [34]. SOC was included in density-of-states (DOS) calculations when comparing directly to PES. Geometry optimization of the reference 0D $MA_3Sb_2I_9$ yielded lattice parameters of a = 8.7404 Å and c = 22.6605 Å. Numerical settings used for geometrical optimization and subsequent electronic structure calculations, including k-meshes and convergence thresholds, are provided in the ESI for full reproducibility

### 2.5. Finite-temperature dynamics and ensemble DOS

*Ab initio* molecular dynamics (AIMD) simulations were performed in the canonical ensemble at 300 K with a Nosé–Hoover thermostat [35,36] on supercells representing 0D and 2D $MA_3Sb_2I_9$ polymorphs, as

well as a hypothetical 3D $MASbI_3$ reference structure. After equilibration, 10 ps production runs were carried out with a 1 fs time step. To ensure computational efficiency during trajectory generation, an electronic energy convergence criterion of $10^{-4}$ eV was employed in the AIMD simulations

From each trajectory, 500 snapshots were sampled to compute the ensemble-averaged DOS via self-consistent calculations including SOC. For these higher-precision SCF calculations, a stricter convergence threshold of $10^{-7}$ eV was applied to ensure accurate electronic properties. A $2 \times 2 \times 1$ *k*-mesh was used in these calculations, and its adequacy was validated by systematic convergence tests, as shown in Fig. S2 in the ESI. Both the total energy and the DOS profile, particularly the relative peak positions, are well converged, supporting the reliability of the chosen numerical settings. This workflow captures thermally averaged electronic properties and the rotational freedom of MA cations that affect local coordination and spectral features.

To further confirm the stability of our AIMD simulations, we examined the total energy evolution during the 10 ps production runs after pre-equilibration for representative pristine and defective systems. As shown in Fig. S3 in the ESI, the total energy fluctuates around stable average values without any systematic drift, confirming that each system reaches a stable equilibrium and that the sampled snapshots provide a reliable representation of the thermally averaged structural states used in the ensemble analysis. These simulations are therefore used to characterize the local structural consequences of Sb deficiency, rather than to track an explicit long-time Sb diffusion trajectory.

### 2.6. Model–experiment linkage

The theoretical analysis was designed to explain the in-situ observations. SOC-included DOS reproduces the PES trends, while AIMD simulations of pristine and Sb-deficient model structures reveal the local structural consequences of Sb depletion, including the collapse of Sb–I coordination and the tendency toward I–I bond formation. These results are consistent with the experimentally inferred irreversible loss of Sb-related spectral signatures during cool-down. Full computational parameters and all input/output files will be available in the ESI

## 3. Results and discussion

To elucidate the temperature-dependent surface evolution of $MA_3Sb_2I_9$, we defined three distinct stages—as-received (pristine $MA_3Sb_2I_9$), after annealing (MA-depleted mixed 0D–2D phase), and after cool-down (Sb-deficient surface with local 3D-like motifs). Annealing enhances surface crystallinity through MA depletion, whereas the subsequent cool-down triggers Sb interdiffusion into the bulk. To capture these sequential yet distinct processes involving MA depletion during annealing and Sb interdiffusion during cool-down, we combined in situ RHEED and high-resolution PES with first-principles calculations. High-quality single crystals with large, flat facets enabled atomically ordered surfaces suitable for surface-sensitive probes, allowing intrinsic temperature-driven changes to be disentangled from artefacts. Experimental observations are presented first, followed by SOC-included DOS and finite-temperature AIMD analyses that reveal the microscopic origins of the irreversible transformation.

### 3.1. Surface structural and electronic evolution under thermal cycling

As mentioned in the Introduction, $MA_3Sb_2I_9$ adopts 0D dimeric [7] and 2D layered [8] frameworks distinct from conventional 3D $ABX_3$ perovskites (Fig. S1a) [37]. The 2D motif may be viewed as a layered derivative from the 3D structure by the removal of one layer of B atoms, while the 0D motif comprises isolated dimers resulting from a different stacking configuration adopted by the X atoms. In both, the MA cations exhibit orientational dynamics at RT that influence finite-temperature properties (Fig. S1a) [22,38]. We grew high-quality single-crystal $MA_3Sb_2I_9$ samples and characterized their surface structures through surface-sensitive probes. We observed clear streak-like RHEED patterns at room temperature after the annealing process (Fig. 1b). Using a calibration factor of 0.049 $Å^{-1}$ per pixel obtained from the Si(111)-(7 × 7) substrate, the streak spacings d1, d2, d3, and d4 with 11, 5, 7, and 7 pixels correspond to reciprocal distances of approximately 0.537, 0.244, 0.342, and 0.342 $Å^{-1}$, respectively. From these periodicities, an apparent surface-projected out-of-plane spacing of about 18.4 Å can be inferred. This value reflects surface-projected vertical periodicity rather than a bulk lattice constant, and is used here solely as a qualitative indicator of surface order. The well-defined streaks confirm that annealing produces a clean, atomically ordered surface suitable for tracking subtle temperature-driven changes using surface-sensitive probes [22]. The availability of such high-quality single crystals comparable to those used in recent lead-free single-crystalline device studies further supports the robustness of our experimental approach [39].

The high-resolution PES experiments were performed to obtain the valence spectra as shown in Fig. 2a. The RT PES in the as-received state shows a broad valence envelope ranged from 15 eV up to energies near $E_F$. Following annealing, all peaks were clearly enhanced, and this result was confirmed by the RHEED experiment. (Fig. 1b) When the clean sample was cooled to the liquid nitrogen temperature (77 K), the valence spectrum exhibited a striking resemblance to that of the as-received sample. Notably, even when the sample was returned to room temperature, no alterations in the valence spectrum were observed. In an effort to generate a new surface, the sample temperature was elevated to 373 K. However, the post-reannealing sample remained unchanged.

The Sb 4*d* core-level spectra also show similar features, as shown in Fig. 2b. In the as-received sample, the Sb core-level spectrum exhibits a very broad peak, suggesting amorphous-like structural disorder within the near-surface region [25,40]. Upon thermal annealing, the spectrum becomes well-defined, indicating the formation of a crystalline structure. Furthermore, the energy shift between the two observed peaks implies a change in the Fermi level has occurred between the two samples [41,42]. A similar observation was made in the valence spectrum, wherein the Sb 4*d* core-level spectra exhibited poor intensity and

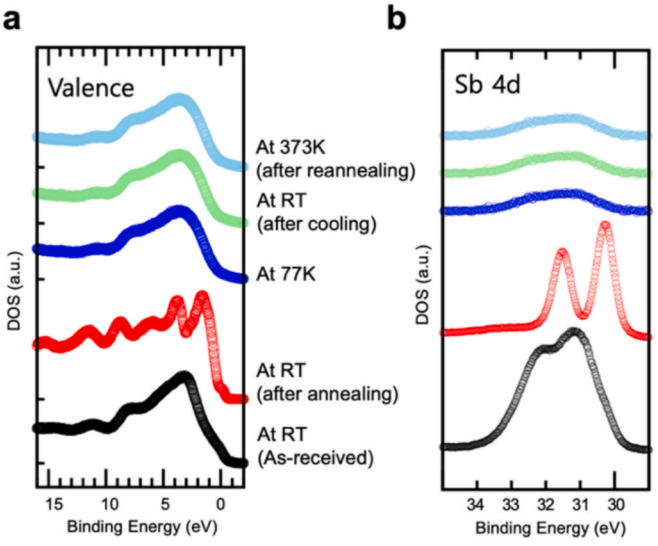


**Fig. 2.** (a) High-resolution PES valence band spectra of $MA_3Sb_2I_9$ recorded at room temperature before annealing (as-received), after annealing, and after cooling to 77 K. The spectra show enhanced peak definition after annealing and a return to a broadened state upon cooling, indicative of irreversible surface modifications. (b) Sb 4*d* core-level spectra for the corresponding thermal conditions, showing clear changes in peak positions and intensities associated with Sb bonding variation and Sb content. These spectral changes support the hypothesis of Sb interdiffusion from the surface into the bulk during the cooling process.

an amorphous-like spectrum following cooling and at room temperature, respectively. This observation may suggest a decrease in the concentration of Sb atoms within the measurement range of PES.

Since this irreversible change occurs during the cooling process, the desorption of Sb atoms from the surface cannot account for the observation because it is energetically unfavorable. Instead, an alternative hypothesis posits interdiffusion of Sb atoms from surface into the bulk [43,44], which may lower the total energy of the entire system and is therefore allowed in the cooling process. This scenario rationally explains the observation in PES measurements and is fundamentally distinct from the prevalent observation of Sb diffusion at high temperature, which is typically attributed to the energetic instability of the atomic structure.

### 3.2. First-principles insight into phase coexistence and Sb interdiffusion

To validate the Sb interdiffusion hypothesis and elucidate its microscopic mechanism, we conducted first-principles calculations based on DFT. These were complemented by AIMD simulations to incorporate the dynamic rotation of MA molecules, critical for realistically capturing the thermally averaged electronic structure, which allows us to reproduce experimental observations. Details of these calculations are provided in the Methods section and the ESI. Fig. S4 shows the variation in DOS with lattice constants, and Fig. S5 presents the rotational dynamics of MA molecules at room temperature. Additional computational parameters can be found in the Methods section.

The PES spectrum of the annealed sample, shown in Fig. 2a, exhibits well-defined features, indicating high crystallinity. Thus, we began by comparing the experimental PES data with ensemble-averaged DOS calculated for both 0D and 2D $MA_3Sb_2I_9$ configurations, as summarized in Fig. 3a. While the 0D phase, which is the most stable configuration, largely reproduces the observed spectral shape, the presence of additional shoulder in the 3–4 eV region in the PES spectrum suggests a mixed-phase nature. In this energy region, the 2D phase exhibits two distinct peaks, whereas the 0D phase does only one. Indeed, the arithmetic average of the DOS from 0D and 2D phases aligns more closely with the experiment, supporting phase coexistence.

However, several prominent peaks, as highlighted with red arrows in Fig. 3a, are absent in the experimental spectra, implying that the surface may host complex states not captured by the bulk structures. Partial DOS (PDOS) analysis shown in Fig. 3b attributed the unmatched peaks to contributions from MA molecules marked by blue shaded regions, implying that post-annealing process induces partial MA depletion [45,46]. To examine this further, we simulated DOS for 0D $MA_{3-x}Sb_2I_9$ with varying degrees of MA deficiency ($x$ = 0.5, 1.0, 1.5) as shown in Fig. 3c. As MA content decreased, the theoretical spectra approached experimental trends, validating the presence of MA-depleted regions after annealing. As expected from the PDOS analysis, the depletion of MA molecules reduces the corresponding peak intensities, thereby resolving the quantitative mismatch between theory and experiments. This indicates that the after annealing sample contains both 0D and 2D structures with a reduced concentration of MA molecules. The coexistence of 0D dimeric units and 2D layered motifs in the annealed state is schematically illustrated in Fig. S6a in the ESI, which provides a simplified structural picture of the mixed surface configuration inferred from the PES–DOS comparison. This observation is consistent with previous reports that organic–inorganic perovskites often undergo surface MA loss during thermal annealing [45,46]. We further note that the complex crystal structure observed in our sample implies a possibility of additional phase evolution during heating and/or cooling process.

To connect the annealing-induced changes with the transformations occurring during cool-down, it is important to consider how the redistribution of volatile and nonvolatile species alters the subsequent surface and bulk responses. The $MA_3Sb_2I_9$ polymorphs (0D and 2D) inherently possess intrinsic Sb layer vacancies, which can provide accessible pathways for Sb migration. In addition, the MA-deficient environment induced by annealing can further facilitate local coordination rearrangement during the subsequent cool-down process. Taken together, these observations suggest that Sb interdiffusion during cool-down is more plausibly described as a vacancy-assisted process accompanied by local coordination rearrangement, rather than as a simple continuation of the annealing-induced surface evolution. These observations indicate that the irreversible evolution observed experimentally arises not from a simple continuation of the annealing process, but from the onset of a distinct structural and stoichiometric reorganization during cool-down.

After the cool-down process, the valence band spectrum became significantly broadened relative to the annealed state, and the Sb 4*d* core level shifted toward lower binding energy, as shown in Fig. 2b, indicating compositional and bonding changes near the surface. These features point to the migration of Sb atoms from the surface into the bulk during cool-down, leaving the topmost region progressively Sb-poor. To understand the structural environment into which the migrated Sb is incorporated, we examined a hypothetical configuration with local 3D-like Sb-I coordination, representing a locally Sb-rich coordination environment analogous to the octahedral networks in conventional $ABX_3$ perovskites. The DOS of this 3D-like configuration, as illustrated in Fig. S1b, exhibits a downward shift of the conduction band relative to pristine $MA_3Sb_2I_9$, consistent with the abrupt spectral evolution observed experimentally.

Sb migration therefore introduces two concurrent but distinct effects: (i) the formation of localized 3D-like coordination within the bulk region that accumulates Sb, and (ii) the development of an Sb-poor surface layer. As schematically illustrated in Fig. S6b, this process gives rise to an Sb-poor surface with increased vacancy density, together with the formation of localized 3D-like bonding networks in the bulk region.

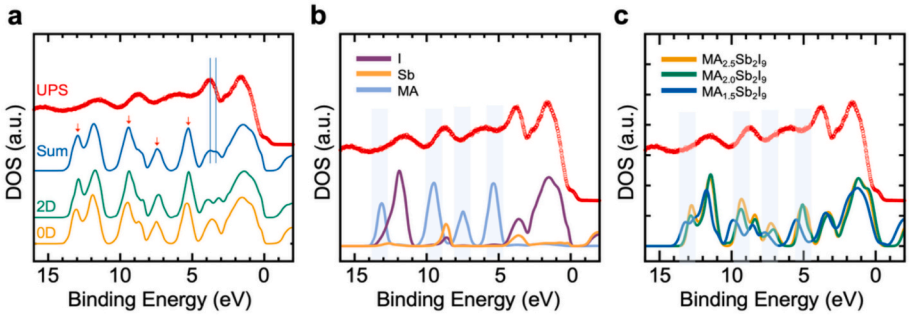


**Fig. 3.** (a) Comparison between the PES spectrum of the annealed $MA_3Sb_2I_9$ sample (red) and the ensemble-averaged DOS from first-principles calculations for 0D (orange) and 2D (green) phases, as well as their arithmetic average (blue). Blue vertical lines and red arrows highlight regions of agreement and discrepancy, respectively. (b) PDOS of the 0D phase, with blue-shaded regions indicating contributions from MA molecules. The suppressed MA-related peaks in the experimental spectrum suggest MA depletion. (c) Ensemble-averaged DOS for 0D $MA_{3-x}Sb_2I_9$ with varying degrees of MA depletion ($x$ = 0.5, 1.0, 1.5), showing improved agreement with PES data as MA concentration decreases, confirming the presence of MA-deficient phases in the annealed sample.

Figs. S6a and S6b together provide a schematic summary of the structural evolution from the mixed 0D/2D annealed surface to the Sb-deficient, locally 3D-like configuration formed after cool-down. When the bulk region with 3D-like coordination and the Sb-poor surface layer are considered together, the characteristic energy shift relative to the aligned Fermi level can be understood as arising primarily from the change in electronic states associated with the 3D-like bonding environment. By contrast, the reduction in Sb-derived spectral weight directly reflects the decreased Sb content at the surface. Taken together, these results show that the irreversible spectral evolution originates primarily from the emergence of 3D-like coordination in the Sb-enriched bulk region, whereas the loss of Sb intensity reflects depletion at the surface. This combined structural and stoichiometric picture reconciles the behaviors observed in the PES spectra and the corresponding theoretical DOS analysis, providing a coherent interpretation of the cool-down driven transformation.

To further validate the Sb interdiffusion mechanism and probe its structural consequences, we compared PES spectra collected before and after the cool-down process. Although the two spectra appear broadly similar at first glance, normalization and differential analysis reveal subtle but significant changes, highlighted by the orange-shaded region shown in Fig. 4a. This region, which is primarily associated with Sb-derived states, exhibits a clear reduction in peak intensity after cooling, indicating the depletion of surface Sb. Among these changes, a distinct shoulder feature near the Fermi level, which is present in the as-received sample, disappears after cooling. Taken together, these spectral signatures are fully consistent with the migration of Sb atoms from the surface into the bulk during cool-down, further supporting the interdiffusion mechanism. To investigate the effects of Sb depletion on the electronic structure, we computed ensemble-averaged DOS for both pristine and 25%-Sb-deficient $MA_3Sb_2I_9$ (i.e., $MA_3Sb_{1.5}I_9$). As shown in Fig. 4b, the difference between these two spectra closely resembles the changes observed in the experimental PES data, particularly in the energy region where the 3.5 eV binding energy peak diminishes and the shoulder near the Fermi level vanishes. Taken together, these spectral signatures strongly support the picture that cool-down drives surface-to-bulk Sb migration, producing an Sb-poor surface and a bulk region with emerging 3D-like coordination. This strong agreement between theoretical and experimental results confirms that Sb interdiffusion leads to a significant redistribution of valence states and plays a central role in driving the observed irreversible transformations.

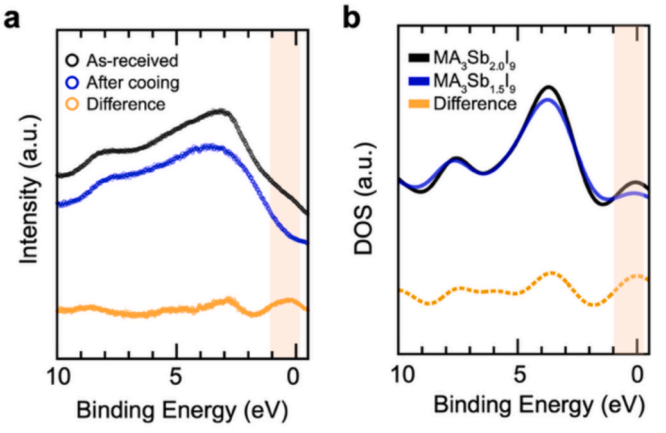


**Fig. 4.** (a) Normalized PES spectra of $MA_3Sb_2I_9$ in the as-received (black circles) and after-cooling (blue circles) states. The difference between the two spectra is indicated by orange circles, with the orange-shaded region highlighting the disappearance of a shoulder near the Fermi level after cooling, suggesting Sb depletion. (b) Ensemble-averaged DOS for pristine (black line) and 25%-Sb-depleted $MA_3Sb_2I_9$ ($MA_3Sb_{1.5}I_9$) (blue line), where the orange dashed line represents their difference. This closely mirrors the spectral deviation observed in (a), supporting the hypothesis that Sb interdiffusion into the bulk during cooling alters the valence electronic structure and introduces irreversibility.

To gain atomistic insight into these irreversible changes, we analyzed the radial distribution functions (RDFs) of both pristine and Sb-deficient structures. As depicted in Fig. 5a, the pristine $MA_3Sb_2I_9$ system exhibits a sharp peak near 3 Å corresponding to robust Sb-I covalent bonding, with no evidence of I-I bonds. In contrast, the Sb-deficient structure shows a weakened Sb-I correlation and the emergence of a new RDF peak at a similar bond length, now associated with I-I bonding, as shown in Fig. 5b. This suggests that removal of Sb from the local environment destabilizes the original bonding network, facilitating the formation of covalent I-I bonds. The energetic strength of these new bonds likely prevents structural recovery during subsequent thermal annealing, thereby explaining the irreversible nature of the surface transformation. These findings emphasize the crucial role of Sb content in governing both the electronic properties and phase resilience of $MA_3Sb_2I_9$ perovskites under thermal stress.

## 4. Conclusion

In this study, we synthesized high-quality single crystals of $MA_3Sb_2I_9$ and conducted a comprehensive investigation into the thermal stability and electronic behavior. Utilizing RHEED and high-resolution PES, we observed that while annealing enhances surface crystallinity and sharpens spectral features, subsequent cooling introduces irreversible surface degradation. This degradation manifests as the loss of Sb-related spectral features and a shift in core-level signals, suggesting a migration of Sb atoms into the bulk.

DFT calculations, combined with *ab initio* molecular dynamics simulations, revealed that $MA_3Sb_2I_9$ accommodates coexisting 0D and 2D structural phases, particularly after annealing. Our simulations further demonstrated that MA molecule depletion contributes to spectral deviations from idealized models. Most notably, the cooling process promotes Sb interdiffusion and results in a surface Sb-deficient state. This transition facilitates the breakdown of the original Sb-I bonding frameworks and the emergence of covalent I-I bonds, which are energetically stable and hinder the reversibility of surface structure.

These findings collectively highlight the intrinsic thermal instability of $MA_3Sb_2I_9$ surfaces and provide atomic-scale insights into the processes responsible for irreversible surface transformations. Understanding the interplay between structural phase evolution, molecular dynamics, and atomic migration offers critical guidance for future design and stabilization of lead-free perovskite materials. Our work underscores the necessity for careful thermal management and surface

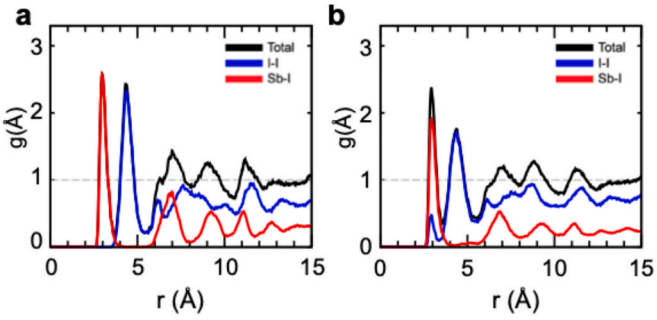


**Fig. 5.** Radial distribution functions (RDFs) of $MA_3Sb_2I_9$ projected onto Sb-I and I-I atomic pairs. (a) In the pristine 0D dimer structure, a strong peak for Sb-I bonding is observed, with no significant I-I interactions, indicating a stable covalent framework. (b) In the 25%-Sb-depleted structure ($MA_3Sb_{1.5}I_9$), the Sb-I peak intensity diminishes, while a new peak corresponding to I-I bonding emerges. This shift signifies the collapse of original Sb-I coordination and the formation of covalent I-I bonds, explaining the irreversible broadening in the PES spectrum and the failure of the surface to recover post-annealing due to the high dissociation energy of I-I bonds.

passivation strategies in advancing $MA_3Sb_2I_9$-based optoelectronic devices toward practical applications.

## CRediT authorship contribution statement

**Seungwoo Yoo:** Writing – original draft, Conceptualization, Visualization, Formal analysis, Data curation. **Young Mi Lee:** Writing – original draft, Formal analysis. **Seungjun Lee:** Writing – original draft, Formal analysis. **Inhee Maeng:** Formal analysis, Data curation. **Jae Ho Kim:** Formal analysis, Data curation. **Yuya Yoshie:** Formal analysis, Data curation. **Sakura Nishino Takeda:** Formal analysis, Data curation. **Masakazu Nakamura:** Formal analysis, Data curation. **Zhe Sun:** Formal analysis, Data curation. **Seung Jae Oh:** Formal analysis, Data curation. **Myungkwan Song:** Formal analysis, Data curation. **Shenghao Wang:** Writing – review & editing, Funding acquisition, Formal analysis, Data curation, Conceptualization. **Min-Cherl Jung:** Writing – original draft, Methodology, Funding acquisition, Formal analysis, Data curation, Conceptualization. **Young-Kyun Kwon:** Writing – review & editing, Writing – original draft, Supervision, Methodology, Funding acquisition, Formal analysis, Data curation, Conceptualization.

## Declaration of competing interest

The authors declare that they have no known competing financial interests or personal relationships that could have appeared to influence the work reported in this paper.

## Acknowledgements

This work was supported by JSPS KAKENHI (grant no. 23K04566, Japan), National Research Foundation of Korea (NRF) grant funded by the Korean government (MSIT) (RS-2022-NR069250, RS-2023-00208792, RS-2024-00416976, RS-2025-25457100), and the National Natural Science Foundation of China (12474072). The computational work was partially done using the resources of the KISTI Supercomputing Center (KSC-2024-CRE-0211, KSC-2024-CRE-0540).

## Appendix A. Supplementary data

Supplementary data to this article can be found online at https://doi.org/10.1016/j.apsusc.2026.166846.

## Data availability

Data will be made available on request.

## References

[1] J. Jeong, M. Kim, J. Seo, H. Lu, P. Ahlawat, A. Mishra, Y. Yang, M.A. Hope, F. T. Eickemeyer, M. Kim, Y.J. Yoon, I.W. Choi, B.P. Darwich, S.J. Choi, Y. Jo, J. H. Lee, B. Walker, S.M. Zakeeruddin, L. Emsley, U. Rothlisberger, A. Hagfeldt, D. S. Kim, M. Grätzel, J.Y. Kim, Nature 592 (2021) 381–385, https://doi.org/10.1038/s41586-021-03406-5.
[2] H. Cho, S.-H. Jeong, M.-H. Park, Y.-H. Kim, C. Wolf, C.-L. Lee, J. Hyuck Heo, A. Sadhanala, N. Myoung, S. Yoo, S.H. Im, R.H. Friend, T.-W. Lee, Science 350 (2015) 1222–1225, https://doi.org/10.1126/science.aad1818.
[3] I. Maeng, Y.M. Lee, M.C. Jung, Small Sci. 4 (2024) 2300186, https://doi.org/10.1002/smsc.202300186.
[4] Z. Yi, N.H. Ladi, X. Shai, H. Li, Y. Shen, M. Wang, Nanoscale Adv. 1 (2019) 1276–1289, https://doi.org/10.1039/c8na00416a.
[5] Z. Shi, J. Guo, Y. Chen, Q. Li, Y. Pan, H. Zhang, Y. Xia, W. Huang, Adv. Mater. 29 (2017) 1605005, https://doi.org/10.1002/adma.201605005.
[6] B. Do Lee, J.W. Lee, M. Kim, W.B. Park, K.S. Sohn, NPJ Comput. Mater. 8 (2022) 34, Doi: 10.1038/s41524-022-00781-z.
[7] D. Ju, X. Jiang, H. Xiao, X. Chen, X. Hu, X. Tao, J. Mater. Chem. A 6 (2018) 20753–20759, https://doi.org/10.1039/c8ta08315k.
[8] N. Giesbrecht, A. Weis, T. Bein, J. Phys. Energy 2 (2020) 024007, https://doi.org/10.1088/2515-7655/ab78ef.
[9] Z. Jin, Z. Zhang, J. Xiu, H. Song, T. Gatti, Z. He, J. Mater. Chem. A 8 (2020) 16166–16188, https://doi.org/10.1039/D0TA05433J.
[10] C. Stecker, K. Liu, J. Hieulle, R. Ohmann, Z. Liu, L.K. Ono, G. Wang, Y. Qi, ACS Nano 13 (2019) 12127–12136, https://doi.org/10.1021/acsnano.9b06585.
[11] Z. Fang, B. Deng, Y. Jin, L. Yang, L. Chen, Y. Zhong, H. Feng, Y. Yin, K. Liu, Y. Li, J. Zhang, J. Huang, Q. Zeng, H. Wang, X. Yang, J. Yang, C. Tian, L. Xie, Z. Wei, X. Xu, Nat. Commun. 15 (2024) 10041, https://doi.org/10.1038/s41467-024-54925-4.
[12] H. Zhao, K. Ma, J. Li, Y. Fu, Y. Qin, D. Zhao, H. Dai, Z. Hu, Z. Sun, H.Y. Gao, Small 18 (2022) 2204271, https://doi.org/10.1002/smll.202204271.
[13] M.C. Jung, A. Matsuyama, S. Kobori, I. Maeng, Y.M. Lee, M. Song, S.H. Jin, M. Nakamura, Sci. Rep. 9 (2019) 11210, https://doi.org/10.1038/s41598-019-47252-y.
[14] A. Hassan, Z. Wang, Y.H. Ahn, M. Azam, A.A. Khan, U. Farooq, M. Zubair, Y. Cao, Nano Energy 101 (2022) 107579, https://doi.org/10.1016/j.nanoen.2022.107579.
[15] L. Zhang, P.H.L. Sit, J. Phys. Chem. C 119 (2015) 22370–22378, https://doi.org/10.1021/acs.jpcc.5b07000.
[16] J. Haruyama, K. Sodeyama, L. Han, Y. Tateyama, J. Phys. Chem. Lett. 5 (2014) 2903–2909, https://doi.org/10.1021/jz501510v.
[17] F. Jiang, D. Yang, Y. Jiang, T. Liu, X. Zhao, Y. Ming, B. Luo, F. Qin, J. Fan, H. Han, L. Zhang, Y. Zhou, J. Am. Chem. Soc. 140 (2018) 1019–1027, https://doi.org/10.1021/jacs.7b10739.
[18] B. Saparov, F. Hong, J.P. Sun, H.S. Duan, W. Meng, S. Cameron, I.G. Hill, Y. Yan, D. B. Mitzi, Chem. Mater. 27 (2015) 5622–5632, https://doi.org/10.1021/acs.chemmater.5b01989.
[19] Y.N. Ivanov, A.A. Sukhovskii, V.V. Lisin, I.P. Aleksandrova, Inorg. Mater. 37 (2000) 623–627, https://doi.org/10.1023/A:1017524618930.
[20] T.D. Chonamada, A.B. Dey, P.K. Santra, ACS Appl. Energy Mater. 3 (2020) 47–55, https://doi.org/10.1021/acsaem.9b01899.
[21] S. Berri, Eur. Phys. J. B 93 (2020) 144, https://doi.org/10.1140/epjb/e2020-10143-1.
[22] I. Maeng, S. Lee, H. Tanaka, J.H. Yun, S. Wang, M. Nakamura, Y.K. Kwon, M. C. Jung, NPG Asia Mater. 12 (2020) 53, https://doi.org/10.1038/s41427-020-0235-6.
[23] I. Maeng, S. Lee, E.Q. Han, Y. Zhang, S.J. Oh, M. Nakamura, J.H. Yun, L. Wang, Y. K. Kwon, M.C. Jung, NPG Asia Mater. 13 (2021) 75, https://doi.org/10.1038/s41427-021-00343-7.
[24] I. Maeng, S. Chen, S. Lee, S. Wang, Y.K. Kwon, M.C. Jung, Mater. Today Phys. 30 (2023) 100960, https://doi.org/10.1016/j.mtphys.2022.100960.
[25] J.F. Moulder, W.F. Stickle, P.E. Sobol, K.D. Bomben, Handbook of X-ray photoelectron spectroscopy a reference book of standard spectra for identification and interpretation of XPS data (1992), Doi: 10.1002/sia.740030412.
[26] P. Hohenberg, W. Kohn, Phys. Rev. 136 (1964) B864–B871, https://doi.org/10.1103/PhysRev.136.B864.
[27] W. Kohn, L.J. Sham, Phys. Rev. 140 (1965) A1133–A1138, https://doi.org/10.1103/PhysRev.140.A1133.
[28] W. Kohn, A.D. Becke, R.G. Parr, J. Phys. Chem. 100 (1996) 12974–12980, https://doi.org/10.1021/jp960669l.
[29] G. Kresse, J. Furthmüller, Phys. Rev. B 54 (1996) 11169–11186, https://doi.org/10.1103/PhysRevB.54.11169.
[30] J. Hafner, G. Kresse, Properties of Complex Inorganic Solids (1997) 69–82, https://doi.org/10.1007/978-1-4615-5943-6_10.
[31] P.E. Blöchl, Phys. Rev. B 50 (1994) 17953–17979, https://doi.org/10.1103/PhysRevB.50.17953.
[32] G. Kresse, D. Joubert, Phys. Rev. B 59 (1999) 1758–1775, https://doi.org/10.1103/PhysRevB.59.1758.
[33] J.P. Perdew, K. Burke, M. Ernzerhof, Phys. Rev. Lett. 77 (1996) 3865–3868, https://doi.org/10.1103/PhysRevLett.77.3865.
[34] S. Grimme, J. Antony, S. Ehrlich, H. Krieg, J. Chem. Phys. 132 (2010) 154104, https://doi.org/10.1063/1.3382344.
[35] S. Nosé, J. Chem. Phys. 81 (1984) 511–519, https://doi.org/10.1063/1.447334.
[36] W.G. Hoover, Phys. Rev. A 31 (1985) 1695–1697, https://doi.org/10.1103/PhysRevA.31.1695.
[37] S.T. Thornton, G. Abdelmageed, R.F. Kahwagi, G.I. Koleilat, J. Chem. Technol. Biotechnol. 97 (2022) 810–829, https://doi.org/10.1002/jctb.6830.
[38] T. Chen, B.J. Foley, B. Ipek, M. Tyagi, J.R.D. Copley, C.M. Brown, J.J. Choi, S. H. Lee, Phys. Chem. Chem. Phys. 17 (2015) 31278–31286, https://doi.org/10.1039/c5cp05348j.
[39] B. Yang, Y.J. Li, Y.X. Tang, X. Mao, C. Luo, M.S. Wang, W.Q. Deng, K.L. Han, J. Phys. Chem. Lett. 9 (2018) 3087–3092, https://doi.org/10.1021/acs.jpclett.8b01116.
[40] M.C. Jung, K.H. Kim, Y.M. Lee, J.H. Eom, J. Im, Y.G. Yoon, J. Ihm, S.A. Song, H. S. Jeong, H.J. Shin, J. Appl. Phys. 104 (2008) 074911, https://doi.org/10.1063/1.2990766.
[41] T. Lei, C. Liu, J.L. Zhao, J.M. Li, Y.P. Li, J.O. Wang, R. Wu, H.J. Qian, H.Q. Wang, K. Ibrahim, J. Appl. Phys. 119 (2016) 015302, https://doi.org/10.1063/1.4939281.
[42] J.W. Kim, S. Kim, J.M. Seo, S.-I. Tanaka, M. Kamada, Phys. Rev. B 54 (1996) 4476–4479, https://doi.org/10.1103/PhysRevB.54.4476.
[43] S. Mizuo, H. Higuchi, Jpn. J. Appl. Phys. 20 (1981) 739–749, https://doi.org/10.1143/jjap.20.739.

[44] S.M. Myers, H.J. Rack, J. Appl. Phys. 49 (1978) 3246–3254, https://doi.org/10.1063/1.325272.
[45] B. Kammlander, S. Svanström, D. Kühn, F.O.L. Johansson, S. Sinha, H. Rensmo, A. G. Fernández, U.B. Cappel, Chem. Commun. 58 (2022) 13523–13526, https://doi.org/10.1039/d2cc04867a.
[46] B. Conings, J. Drijkoningen, N. Gauquelin, A. Babayigit, J. D'Haen, L. D'Olieslaeger, A. Ethirajan, J. Verbeeck, J. Manca, E. Mosconi, F. De Angelis, H. G. Boyen, Adv. Energy Mater. 5 (2015) 1500477, https://doi.org/10.1002/aenm.201500477.